Advanced quantification for single-cell adhesion by variable-angle TIRF nanoscopy

Dalia El Arawi, Cyrille Vézy, Régis Deturche, Maxime Lehmann, Horst Kessler, Monique Dontenwill, Rodolphe Jaffiol

Advanced quantification for single cell adhesion by variable-angle TIRF nanoscopy

Dalia El Arawi[1], Cyrille Vézy[1], Régis Déturche[1], Maxime Lehmann[2], Horst Kessler[3], Monique Dontenwill[2] and Rodolphe Jaffiol[1,*]

[1] Light, nanomaterials, nanotechnologies (L2n), ERL CNRS 7004, Université de Technologie de Troyes, 12 rue Marie Curie, CS 42060, 10004 Troyes cedex, France.
[2] Laboratoire de Bioimagerie et Pathologies (LBP), UMR CNRS 7021, Université de Strasbourg, Faculté de Pharmacie, 74 route du Rhin, CS 60024, 67401 Illkirch cedex, France.
[3] Institute for Advanced Study (IAS), Technische Universität München, Department Chemie, Lichtenbergerstrasse 4, Garching, Germany.

[*]Correspondence: rodolphe.jaffiol@utt.fr

ABSTRACT

Over the last decades, several techniques have been developed to study cell adhesion, however they present significant shortcomings. Such techniques mostly focus on strong adhesion related to specific protein-protein associations, such as ligand/receptor binding in focal adhesions. Therefore, weak adhesion, related to less specific or non-specific cell/substrate interactions, are rarely addressed. Hence, we propose in this paper a complete investigation of cell adhesion, from highly specific to non-specific adhesiveness, using variable-angle Total Internal Reflection Fluorescence (vaTIRF) nanoscopy. This technique allows us to map in real time, cell topography with a nanometric axial resolution, along with cell cortex refractive index. These two key parameters allow us to distinguish high and low adhesive cell/substrate contacts. Furthermore, vaTIRF provides cell/substrate binding energy; thus, revealing a correlation between cell contractility and cell/substrate binding energy. Here, we highlight the quantitative measurements achieved by vaTIRF on U87MG glioma cells expressing different amounts of α_5 integrins, and distinct motility on fibronectin. Regarding integrins expression level, data extracted from vaTIRF measurements, such as the number and size of high adhesive contacts per cell, corroborate the adhesiveness of U87MG cells as intended. Interestingly enough, we found that cells overexpressing α_5 integrins, present a higher contractility and lower adhesion energy.

INTRODUCTION

Adhesion is crucial for many cellular activities. It is involved in essential physiological cell function (survival, proliferation, migration, differentiation...), as well as pathological conditions (inflammation, metastasis...). Cell plasma membrane and its adjacent cortex are two key components implicated in adhesion. They form a substantial meshwork whose study is critical. However, our ability to understand these important regions is limited by our ability to observe them in detail within living cells.

Cell adhesion is furthermore a multiparameter phenomenon, which can be addressed in different ways, from the nanoscale, typically on focal adhesions (FA), to the cell scale. Numerous techniques are currently used to study adhesion at the single cell level. Regarding all-optical approaches, super-resolution techniques became more and more popular in recent years. These new nanoimaging techniques yielded tremendous relevant observations of focal adhesions. Single molecule localization and stimulated emission depletion (STED) nanoscopies were employed for instance, to reveal that β_1-integrins nanoclusters, appearing in FA, are subdivided into two groups where integrins are either active or inactive (1). Interferometric photo-activated localization microscopy (iPALM) allows impressive observations of FA units by providing their protein 3D-architecture at the nanoscale (2) (3). Structured illumination microscopy (SIM) combined with total internal reflection fluorescence (TIRF) microscopy has been used to reveal the growth dynamics of linear subunits which form the focal adhesion plaques (4). Moreover, single molecule tracking can also yield interesting information about adhesion protein dynamics, such as integrins (5) (6). Traction forces heterogeneity within FA was also highlighted with molecular fluorescent-based nanobiosensor (7). Many other techniques are commonly used to probe cell adhesion, such as traction force microscopy (TFM) (8), reflection interference contrast microscopy (RICM) (9), flow chamber (10), atomic force microscopy (AFM) (11), magnetic tweezer (12), etc.

Despite the great progress that has been made so far with these techniques, and their huge forthcoming insights, most of standard and up-to-date methods useful to study cell adhesion present a major drawback: only highly specific adhesion related to protein-protein recognition can be studied, for instance ligand/receptor binding appearing in focal adhesion plaques. But less specific and non-specific cell/substrate interactions play also a crucial role in cell adhesion, as various cell behaviors seem to suggest, such as during amoeboid motility, where cells can move in the absence of FA (13). A recent publication has shown that specific and non-specific interplay involved in cellular adhesion appears to have a cooperative action. For example, the repulsive non-specific force induced by the glycocalyx can alter the integrin-based focal adhesion plaques and promote cellular migration (14). Cell/substrate interactions include a lot of different non-specific forces: polymer steric repulsion, electrostatic attraction or repulsion, polyelectrolyte-like repulsion (a mix of electrostatic and steric repulsion), van der Waals attraction, Helfrich repulsion (which gives rise to membrane undulations), or friction force (involving transmembrane proteins or lipids) mediated by the retrograde actin flow in the cell cortex. Moreover, some transmembrane proteins such as proteoglycan (e.g., syndecan, CD44) have also an ambivalent behavior. They both induce a non-specific steric repulsion due to their long oligosaccharide chains, and their herapan sulfate (HS) side chains enables specific binding on extracellular matrix proteins such as fibronectin (15). In this case, the frontier between specific and non-specific interactions is tenuous, and so difficult to decipher. In addition to this complexity, cell/substrate adhesion can be also altered by some “external” forces, i.e., not associated to membrane components only. This "external" force can be related to cell contractility driven by myosin motors within actin filaments. To conclude, there is a large panel of specific and non-specific forces occurring in cell adhesion, and some of these forces are still poorly studied and understood.

There is a significant difference between specific and non-specific adhesion. Specific interactions present in FA give rise to a strong adhesion, i.e. characterized by an important ligand/receptor binding energy (10) (11) (16). At the opposite, it is commonly assumed that outside FA, cell/substrate interactions are weaker, but this was only demonstrated on biomimetic system with giant unilamellar vesicles (17), and never on living cells. Furthermore, familiar immunofluorescence pictures of FA as linear sub-diffractive structures, represent only a slight fraction of the cell/substrate contact (Figure S1). So, even though non-specific and weak interactions are locally low or negligible, their relative weight at the cell scale could be significant.

Therefore, they might have an important physiological role in cell adhesion in the same way as high specific contacts.

In this paper, we propose a promising single cell quantitative imaging technique yielding to study simultaneously regions of high and low cell adhesiveness. This method was based on a recent upgrade of variable-angle Total Internal Reflection Fluorescence (vaTIRF) nanoscopy, as previously proposed (18). Our improved vaTIRF strategy is based on a dual measurement: the membrane height *h* with a nanometric axial resolution (typically 10-20 nm), similar to the one achievable with other methods of nanoscopy (2) (19) (20) (21) (22) (23), and the cell cortex refractive index, denoted n_{cortex}. This (h,n_{cortex})-dual measurement provides the opportunity to distinguish strong and weak cell/substrate interplay, identifying high adhesive contacts (HAC) and low adhesive contacts (LAC) without any selective immunolabeling or fluorescent fusion proteins. Valuable information can be then extracted in real time on living cells, such as the amount, the size and the spatial distribution of HAC and LAC, and more interestingly their binding energies. This work was conducted using U87MG glioma cell line, which endogenously expresses $\alpha_5\beta_1$ and $\alpha_v\beta_3/\beta_5$ integrins. U87MG cells were previously manipulated to increase or decrease the expression level of α_5 integrin subunit, to provide two sub-cell lines, denoted respectively α_{5+} and α_{5-} (24). U87MG α_{5+} and α_{5-} cells were used because they present a different adhesion and motility on fibronectin, as previously shown with common techniques such as cell adhesion assay and single cell tracking (25). At first, vaTIRF investigations were conducted on α_{5+} and α_{5-} cells to further expand our knowledge about these cell lines. Later on, cells overexpressing α_5 were treated either with actin drugs: a Rho-kinase inhibitor (Y27632) or activator (lysophosphatidic acid, LPA) in order to suppress or improve actin-based cell contractility, or with integrin antagonists to inhibit integrins/surface binding. In addition, different analyses were performed on fixed cells, in order to compare our vaTIRF measurements on living cells with more common ones obtained in immunofluorescence.

MATERIALS AND METHODS

Cell culture

U87MG human malignant glioma α_{5+} and α_{5-} cells were prepared as described in reference (24). α_5 integrin subunit expression was verified by western blot analysis and flow cytometry (25): α_5 integrin is boosted in α_{5+} cells, and inhibited in α_{5-} cells. At the opposite, α_v, β_1, $\alpha_v\beta_3$ and $\alpha_v\beta_5$ integrin expression levels are similar in both cell line (25). U87MG cells were grown in Minimum Essential Medium Eagle (EMEM, Lonza) supplemented with 10% of fetal bovine serum (FBS, Gibco) and 1% of antibiotics/antifungal mixture (penicillin, streptomycin, amphotericin B; Lonza) in a humidified atmosphere at 37°C with 5% CO_2. For vaTIRF measurements, cells were observed in a nonfluorescent culture medium at 488 nm. We used $DMEM^{gfp}$–2 medium (Dulbecco's Modified Eagle Medium, Evrogen) supplemented with L-glutamine at 2 mM (Gibco), HEPES buffer at 20 mM (Gibco), and only 1% of FBS.

Substrate preparation

To observe specific adhesion, we prepared glass surfaces coated with a thin layer of fibronectin. Thickness-corrected glass coverslips were used as substrate ((170 ± 10) µm, Assistent). The coverslips were firstly cleaned by immersion into freshly prepared piranha solution for 1 h (50 % H_2O_2 + 50% H_2SO_4). The coverslips were then rinsed with ultra-pure water and dried. Afterwards, coverslips were incubated in a solution of fibronectin (fibronectin from human plasma at 0.1%, F0895, Sigma-Aldrich) diluted in PBS at 10 µg/mL during 1h. Finally, to remove the non-adsorbed fibronectin, coverslips were rinsed with ultra-pure water and dried again. Glass surfaces coated with RGD peptide motif were also prepared. Coverslips were firstly cleaned by immersion in the ultrasonic bath for 5 min in a water/ethanol (30/70) solution. Coverslips were then rinsed with ultrapure water and dried. Afterwards they were activated in the UV-Ozone cleaner for 5 min and were incubated 1h with a solution of PLL-PEG-RGD at 0.15 mg/mL (PLL(20)-g[3.5]-PEG(2)/PEG(3.5)-RGD, Sussos) in HEPES at 10 mM and NaCl at 150 mM (pH=7.4). Coverslip were then rinsed with ultrapure water and dried.

About n_{cortex} calibration, MY133-MC layer was obtained by dip-coating (26). After cleaning with ultrasonic bath and activation with UV-O_3 cleaner, coverslips were coated with MY133-MC polymer (My Polymer) solution at various concentration, diluted in Novec7100 (3M) (dip coating speed is fixed to 55 mm/min). After dip coating the coverslips were immediately left to cure several hours at room temperature and relative humidity. The layer thickness was measured with an ellipsometer (IPSO 200, PhaseLab Instrument). The quantum dots monolayer was obtained by spin coating. Colloidal QDs (home-made CdSe/ZnS core/shell nanoparticles) in toluene were mixed with PMMA [poly(-methyl methacrylate), MW = 350 kg/mol, 04554-500, Polysciences)] and then spin coated on a coverslip to obtain a thin layer of polymer (thickness ≈10 nm) highly doped with QDs. The PMMA concentration is about 3 g/L and the spin coater rotational speed of 3000 rpm during 5 min.

Pharmacological drugs

Pharmacological reagent Y27632 dihydrochloride (TOCRIS, 1254, Bio-techne) was added to the nonfluorescent culture medium at 50 µM (Y27632 was prediluted in PBS). LPA molecule (Oleoyl-L-α-lysophosphatidic acid, L7260, Sigma) was added in a serum-free nonfluorescent medium at 50 µM (LPA was prediluted in a solution of HEPES at 10 mM and NaCl at 100 mM). Integrin antagonist FR synthesis and affinities have been described elsewhere and correspond to compound 1 in (25) and (27). SN antagonist corresponds to compound 3 in (25) and in (28). They were both diluted in DMSO, and added to the nonfluorescent culture medium at a final concentration of 20 µM. For drug treatment, cells were resuspended in a drug containing medium, then plated on the substrate before vaTIRF observations.

Membrane labeling, immunofluorescence

For plasma membrane labeling, we used the well-known DiO probe (3,3'-dioctadecyloxacarbocyanine perchlorate, $DiOC_{18}(3)$, D275, Invitrogen-ThermoFisher). Membrane labeling was performed as previously described (18).

For experiments on fixed cells, U87MG cells were fixed after being seeded on fibronectin. Firstly, the medium was removed and afterwards slides were incubated with warm 3.7 % paraformaldehyde in PBS (Paraformaldehyde, 16% w/v, methanol free, 43368, Alfa Aesar) and left for 10 min at room temperature. Then samples were washed three times with PBS, and further permeabilized using one of the two detergents Triton X-100 (0.1%) and saponin (0.1%) at room temperature during 1h. For cytoskeleton labeling, cells were incubated in a solution of phalloidin conjugated with Alexa568 dye at 0.33 µM (AlexaFluor 568 Phalloidin, A12380, Invitrogen-ThermoFisher) for 40 min in 0.1% saponin and 1 % BSA in PBS at room temperature. Finally, after several washings, cells were incubated for 2 min in a solution of 1 % paraformaldehyde in PBS. The sample was then stored in PBS for imaging on the same day. All the solutions used for fixation and permeabilization were filtrated (0.2 µm).

vaTIRFM and RICM imaging

After labeling, U87MG cells were placed into a homemade hermetic chamber (to avoid evaporation) made with two coverslips and dedicated to optical observations. The lower coverslip was previously coated with fibronectin. To promote cell adhesion, the sample was incubated for 1 h at 37°C in the presence of 5 % of CO_2. Next, vaTIRF observations were done during the first hour after incubation at 37°C.

vaTIRF experimental setup is detailed in reference (18). The most significant part of our TIRF setup is a mirror mounted onto a motorized rotation stage outside the microscope. It allows us to adjust precisely the incident angle in the sample by tilting the mirror. The working range is from 0° (epi-fluorescence) to ≈ 72°. Different TIRF 60x Olympus objectives were used, with NA from 1.45 to 1.49. The calibration procedure required to establish the magnification relationship between the mirror tilting and the incident angle on the glass/water interface is detailed in a previous publication (29). As a result, the incident angle can be continuously tuned with an accuracy of ≈ 0.1°. Two different laser excitations were used: $\lambda = 488$ and 561 nm. The laser irradiation within the sample is about few W/cm^2 and vaTIRF acquisition rate ≈ 1 s for the image stack. The fluorescence signal from the sample was recorded with a sensitive CMOS camera (ORCA Flash 4.0, Hamamatsu). A fine achievement of the axial focusing was provided by a z-piezo device supporting the objective (Physik Instrumente). At last, the microscope was enclosed in a hermetic controlled temperature chamber to make observations at 37°C.

Reflection Interference Contrast Microscopy setup is similar to the one proposed by J. Radler and E. Sackmann (30). We used the antiflex Zeiss objective (NA = 1.25) with red LED source of light ($\lambda \approx 630$

nm) and a 14-bit CCD detector (LUMO Retiga, Photometrics). This setup enables living cells observations at 37°C.

Statistical analysis

Statistical significance was determined according to *Wilcoxon-Mann-Whitney* rank test and performed with in-built routine in IgorPro (Wavemetrics).

RESULTS AND DISCUSSION

High and low adhesive contacts hypothesis

A typical vaTIRF measurement of a U87MG living cell adhered on glass coated with fibronectin is shown in Figure 1. vaTIRF data acquisition and data processing were described in detail in a previous publication (18). Briefly, by observing only the cell membrane in contact with the substrate (through a simple plasma membrane fluorescent labeling with DiO, Figure 1A), we have demonstrated that a stack of 10 different TIRF images recorded by gradually increasing the incident angle of the laser beam on the sample at the acquisition rate of ≈ 1 s, allows to reconstruct the cell membrane topography of adhesive cells with a nanometric axial precision (Figure 1B). vaTIRF also permits to map the effective refractive index, n_{eff}, of the cell within the evanescent field. n_{eff} mainly depends on two parameters: the local refractive index of the cell cortex, n_{cortex}, and the water gap thickness h between the cell membrane and the substrate. Theoretically, n_{eff} will increase together with n_{cortex}, but also when h decreases, according to the asymptotic trend: $n_{eff} = n_{cortex}$ when $h = 0$ (18). We propose in this paper a calibration of the refractive index, to convert n_{eff} into n_{cortex}, and thus obtain a new picture of the refractive index of the cell cortex (Figure 1C). This requires a multi-layer system preparation that mimic the local refractive index z-stratification within the sample (Figure S2A). The 3-layer stack system used is composed by: a first polymer layer (MY-133-MC) which has the same refractive index as the culture medium, a second layer of emitters (a monolayer of quantum dots in PMMA) mimicking the labeled plasma membrane, and a third layer of various water/glycerol mixture of refractive index n_3 representing the cell cortex (Figure S2A). Since we are able to control precisely the MY-133-MC layer thickness by dip-coating (26) and the refractive index value of water/glycerol mixture (29), we can measure n_{eff} variation for different MY-133-MC gaps and various n_3. It appears that for a given n_3, the n_{eff} values obtained with vaTIRF are similar regardless of the thickness range (50-150nm) of the MY-133-MC layer. Thus, for each water/glycerol mixture on the top layer, we decided to take the average of n_{eff} values measured for three different MY-133-MC gaps (50, 100 and 150 nm). As intended, Figure S2B shows that n_{eff} increases along with n_3, even though the measurement accuracy is debatable. These data can be fitted with a saturation-like function, thereby providing an analytical expression to transform n_{eff} into n_{cortex} (Figure S2). According to this calibration, it becomes possible to compute a new image displaying n_{cortex} instead of n_{eff} (Figures S2C and S2D).

As expected, living cells do not make a flat contact on a glass substrate coated with fibronectin, and numerous tight adhesion zones appear at different places (see the dark blue regions corresponding to $h \lesssim$ 50 nm on Figure 1B). It is well-known that ligand/receptor interplay, such as integrin-fibronectin binding, affects significantly the height of the membrane in 2D. As a result, the membrane most closely approaches the substrate on focal adhesion zones (2) (3) (14) (31). Furthermore, the functional unit of focal contacts includes a cluster of different proteins (integrin, paxillin, talin, FAK, actin...), more or less organized in multi-layers (2). This suggests a significant increase of the local refractive index in the cell cortex n_{cortex}, as proposed for the first time by Izzard et al. (32) (33) and Bereiter-Hahn et al. (34). Hence, focal adhesion regions should appear where the plasma membrane closely approaches the substrate, and the cortex refractive index is high. These two key observations constitute the starting point of this study, paving the way to localize FA without any specific labeling. Hence, zones where plasma membrane is very close to the surface and the effective refractive index is high (typically $h \lesssim 70$ nm and $n_{cortex} \gtrsim 1.37$), must include highly specific cell/substrate contacts, such as focal adhesion plaques, and corresponds to HAC zones. HAC zones can be located by applying a dual thresholding on both h and n_{cortex} images, as shown in Figure

1D. Therefore, high adhesive contacts appear in red in this new two-color image. The rest of the cell is then supposed to include weaker adhesive contacts, LAC zones, forming the blue background in Figure 1D. One can also apply a single thresholding regarding the refractive index n_{cortex} ($n_{cortex} \gtrsim 1.37$), to separate HAC and LAC on the membrane/substrate distance histogram (Figure 1E, same color code).

In order to prove that n_{eff} increase is due to a local protein densification, we decided to observe actin cytoskeleton and compare its spatial distribution with high n_{eff} zones recorded in vaTIRF (in fact, actin filaments form very dense and large structures that exhibit a high refractive index of ≈ 1.56 (35)). For these first investigations, vaTIRF measurements were performed on fixed U87MG α_{5+} cells, where plasma membrane was labeled with DiO and F-actin with Alexa568-phalloidin (note that all other data presented in this paper were strictly conducted on living cells). Firstly, it should be noted that cell fixation and membrane permeabilization damage the plasma membrane by removing many of its components (36) (37). vaTIRF imaging is therefore tricky, because fixed cells present many holes in their plasma membrane, as shown in Figure S3. Nevertheless, using saponin instead of Triton X-100 for membrane permeabilization, allows better vaTIRF analysis. Secondly, these membrane alterations consecutive to fixation and permeabilization, lead to an important reduction of the membrane height h (the mean membrane/substrate distance measured on U87MG α_{5+} living cells was $\langle h \rangle$ = 148 nm, and on fixed cells $\langle h \rangle$ = 77 nm). Moreover, the nucleus becomes visible on many TIRF images (Figures S3 and S4A), suggesting that it is closer to the surface, like another intracellular component such as endoplasmic reticulum, or Golgi apparatus. These outcomes give rise to a global increase of n_{eff} in an artificial way over the whole spreading area, and so a bigger HAC surface. Despite these two drawbacks, analysis of 31 different fixed cells indicated that 42 % (±12 %) of high refractive index zones ($n_{eff} \geq 1.39$) overlap actin rich structures (stress fibers, lamellipodia...), as shown in Figure S4E. This reasonable overlap between n_{eff} and actin cytoskeleton, despite the anomalous increase of n_{eff} previously mentioned, proves a certain correlation between the effective refractive index and the packing of adhesion proteins, such as actin (indeed, actin is not the only component contributing to this n_{eff} increase, many other proteins are as well implicated in cell/substrate interactions).

Membrane height appears to be a non-relevant parameter to distinguish adhesiveness

Typical vaTIRF investigations on U87MG α_{5+} and α_{5-} living cells in adhesion on fibronectin are given in Figure S5. One can recognize the typical morphology of motile cells, which exhibit several close contacts on protrusive edge. Few tens different cells were studied, and several information can be extracted from such experiments. Cell/substrate contact areas were determined with TIRF images (e.g., Figures S2A and S2F). High adhesive contacts were assessed according to the dual thresholding $h \leq 70$ nm and $n_{cortex} \gtrsim$ 1.37-1.38, this last value may change a little bit between cells (e.g., Figures S2D and S2I). Histograms of membrane/substrate separation distance h can be obtained from the cell topography, as well as HAC and LAC h–distance histograms according to the thresholding $n_{cortex} \gtrsim$ 1.37-1.38 (e.g., Figures S2E and S2J).

Figures 2A and 2B show the mean membrane/substrate distance distribution recorded at the single cell level for both cell lines. Their asymmetric profiles exhibit a shoulder for $h \approx 75$ nm, more pronounced for α_{5+} cells, probably due to a higher amount of HAC. Despite this distinction, quantitative analysis of the mean height $\langle h \rangle$ did not reveal any significative variation among α_{5+} and α_{5-} cells (Figures 2C, D and E). This means that height analysis will not provide relevant information about cell adhesion, that would distinguish between these cell lines. This result is very important because it illustrates the benefit of the dual thresholding. This processing, which takes into account the refractive index n_{cortex} in addition to the height h, allow us to go further and evaluate new parameters such as the number and size of HAC and their binding energy.

High and low adhesive contacts increase with integrin expression

TIRF measurements indicate that cell spreading area is larger for α_{5+} cells than α_{5-} cells (Figure 3A). Furthermore, Figures 3B and 3C indicate that this distinct spreading is not only related to highly adhesive contacts, but also affecting low adhesive contacts. Average HAC area plotted on the Figure 3B confirms what has already been visible in Figures 2A and 2B: the cell line overexpressing α_5 integrin subunit,

displays as expected, a bigger HAC area per cell. It is very important to note that such high adhesive contacts only represent a small fraction of the cell/substrate spreading area: 6.8 % (± 3.2 %) for α_{5+} cells and 2.7 % (± 2.5 %) for α_{5-} cells. This highlights that most of cell/substrate interactions are not highly specific, and at first glance, the drastic reduction of low adhesive contact area concerning α_{5-} cells (Figure 3C) means that weaker specific and non-specific interactions are also affected by integrin expression levels.

The larger area of HAC observed for α_{5+} cells may have two different sources: either there is a higher number of HAC, or their size is bigger! To clarify this point, the number and the size of high adhesive contacts were assessed at the single cell level. It appears that there is ≈ 3 times more HAC on a single α_{5+} cell than on α_{5-} cell (Figure 3D). Regarding the size of HAC, there is no significant difference between both cell lines (Figure 3E). Most of HAC patches are smaller than 1 μm^2, but it is not rare to find bigger ones with a size between 1 and 10 μm^2. Both results clearly reveal that HAC number per cell increases in parallel with the integrin expression level. This finding is consistent with measurements obtained with a more routine technique. The latter consists of quantifying FA plaques number by immunofluorescence on fixed cells (Figure S1). However, our vaTIRF method offers a strong benefit: it allows us to probe focal adhesions (or to a large extent cell/substrate specific interactions) on living cells, without any complex labeling that could perturb protein function.

HAC and LAC binding energy decreases with integrin expression

We have previously demonstrated that h–distance distributions (Figure 2) can be used to obtain the potential energy $V(h)$ (also known as the free energy of interactions) related to cell/substrate interactions (38). This potential energy profile $V(h)$ gives an access to the binding energy D_e (or dissociation energy) related to these interactions. This requires to fit the anharmonic potential $V(h)$ with the P. Morse function, thus providing D_e in Joule, or in k_BT unit (D_e corresponds to the depth of the potential well, as shown in Figure 4A). D_e represents an average of the binding energy over the cell spreading area. It is however possible to calculate a binding energy per unit area, denoted D_S, in J/m^2, given by D_e divided by the HAC or LAC area per cell (Figures 3B and 3C).

Two main results appear in Figure 4, making binding-energy a key parameter to quantify the adhesion of motile cells. First of all, binding energies are always smaller for α_{5+} cells, for any kind of cell/substrate interactions (HAC or LAC). This means that α_{5+} cells present a low energy of adhesion. Secondly, and more importantly, we have found that HAC binding energy per unit area D_S is one order of magnitude higher than LAC. This particular finding definitively proves that HAC is related to a strong adhesion process associated with highly specific cell/surface interactions, whereas LAC can be attributed to a weak adhesion process associated with weak and non-specific cell/surface interactions. This confirms older adhesion energy measurements obtained by the group of E. Sackmann with RICM on giant vesicles, exhibiting specific adhesive plaques surrounded by non-specific repulsive zones (17). It also seems clear that, although the binding energy values per unit of surface for LAC are very low ($D_S \approx 10^{-10}$ J/m^2) compared to HAC values ($D_S \approx 10^{-9}$ J/m^2), the resulting contribution of non-specific adhesion at the cell scale is important due to the prominence of LAC area ($D_e \approx$ 15-20 k_BT for LAC and 8-10 k_BT for HAC). These observations highlight, yet again, the crucial role of cell/substrate weak interactions, and also non-specific ones, in cell adhesion.

The low adhesion energy recorded on α_{5+} cells, must be discussed according to their migration capacity. In fact, several publications have shown that migration speed increases with $\alpha_5\beta_1$ integrin expression level on 2D substrate and in 3D microenvironment (25) (39) (40) (41) (42). We did cell tracking measurements on fibronectin and we obtained a 2D random velocity of ≈ 7 µm/h for α_{5+} cells, and ≈ 4 µm/h for α_{5-} cells. Thus, our results indicate that α_{5+} cells move a little bit faster in correlation with a smaller energy of adhesion. This finding corroborates previous observations on a more basic system: MDA-MB-231 cells in adhesion on fibronectin vs on poly-L-lysine (38). Cells adhered on poly-L-lysine exhibit higher adhesion strength and therefore are glued to the substrate. On the contrary, cells on fibronectin exhibiting a smaller adhesion energy can migrate. Fast migration of low adhesive cells was also revealed by the group of M. Piel under conditions of spatial-confinement (13). Furthermore, the increase of cell speed along with a

reduced adhesion is predicted by the mesenchymal-type migration model proposed by DiMilla *et al.* in the early 90s (43), and experimentally verified few years later by Palecek et al. (39). This model envisages a bell-shaped relationship between cell speed and adhesion, with a maximum speed that separates cell adhesivity in two regimes. At low adhesivity, the cytoskeleton contraction dissociates the few numbers of focal adhesions at the front and the rear of the cell, and a net cell displacement occurs. In this first regime, the cell speed increases with adhesiveness. After the maximum, the high adhesivity regime is characterized by a decrease of cell speed as adhesiveness increases. This second regime corresponds to our experimental observations, where there are many FA, especially at the rear of the cell. Therefore, additional bonds formed there, can better withstand contractile forces mediated by the cytoskeleton. Cell translocation and speed are thus decreased with increasing adhesiveness. Live-cell observations of U87MG α_{5+} cells moving on fibronectin revealed the particular mesenchymal-type motility of such cells (RICM movie in the Supporting Material). U87MG α_{5+} cell exhibits multiple protrusive edges, which delay the cell body translocation. Before translocation, many well-defined close contacts (dark area on RICM images) appear at different cell protrusions, resulting in a high level of attachment. These contacts are maintained for a long time under contraction, thus limiting the cell displacement.

Impact of cell contractility on binding energy

To highlight the influence of cell contractility on the potential energy, we evaluated the $V(h)$ profile in presence of a traction force that pulls up a lipid membrane. For this numerical simulation, we applied a traction force F on a lipid bilayer, which exhibits some repeller molecules (such as glycocalyx present on the cell surface), in interaction with a glass surface (Figure 5A). This simulation confirms the crucial role of the additional intracellular contractile force F on $V(h)$: the negative work of the traction force ($-F \times h$) reduces the binding energy D_e (44). In order to confirm this prediction, further experiments were performed on U87MG α_{5+} living cells treated with two different drugs acting on RhoA-associated kinase, and thus on actomyosin based cell contractility: one inhibitor (Y27632) (45) and one activator (LPA, lysophosphatidic acid) (46). Few tens different living cells have been studied for each molecule. Figure S6 shows the expected effects of these drugs on actin cytoskeleton. Regarding Y27632, untreated cells exhibit a lot of stress fibers marked by bright filaments and some large lamellipodia protrusions, characterized by a more diffused signal at some edge (Figure S6A). After treating cells with Y27632 most of stress fibers have disappeared, and sometimes, and an increase in lamellipodia has been observed (Figure S6B). On the other hand, cells to be treated with LPA were cultivated in a serum-free medium. These cells display a very low amount of stress fibers (Figure S6C). Therefore, under serum-free conditions, addition of LPA induced efficiently actin polymerization and many stress fibers can be observed again (Figure S6D).

Results on Figures 5B-G confirm our prediction regarding the influence of the intracellular contractile forces. Y27632-induced reduction of cellular contractility gives rise to an increase of the binding energy D_e (Figures 5B-D), which is due to a reduction of the traction force (Figure 5A). Similar results were previously obtained by traction force microscopy (47). At the opposite, the activation of RhoA signaling pathways with LPA highlights a decrease of D_e (Figures 5E-G), connected to the presence of more myosin motors engaged in actin structures, therefore creating new contractile elements or enhancing those already existing. $V(h)$-profiles plotted in Figures 5B and 5E show that contractile force inhibition or activation is more pronounced for HAC, as confirmed by similar observations achieved with FRET-based force probe microscopy (7), where Y27632 and LPA treatment extinguished or strengthened the local traction force appearing within or near focal adhesion plaques. However, LAC are also affected by cell contractility, because myosin contractile elements are not present only in the stress fibers connected to FA, but also in the cell cortex connected to the plasma membrane (48). In fact, actin cortex is characterized by its tension which can be measured by AFM or micropipette aspiration. This tension is connected to myosin activity and hindering this activity by adding an inhibitor such as Y27632 or Blebbistatin reduces the cortical tension (49) (50). This result suggests that the traction forces induced by contractile elements present in the cell cortex, would be more visible in low adhesive contacts.

The outcomes of U87MG α_{5+} cells treated with Y27632 or LPA offer an interesting perspective to interpret binding energy variations between α_{5+} and α_{5-} cells (Figure 4). Therefore, one can suppose that the decrease of both HAC and LAC binding energies of α_{5+} cells is associated with a higher cell

contractility. The low binding of α_{5+} cells is thus related to a greater cell contractility, which is a hallmark of a higher motility (13). Moreover, the recent work of Chowdhury et al. provides an interesting finding regarding cell spreading and contractility (51). The authors demonstrate that cell spreading is governed by traction forces across single integrins. So, in agreement with these observations, U87MG α_{5+} cells exhibiting more integrins, more HAC (Figure 3D) and higher HAC contractility compared to α_{5-} cells, are obviously more spread out (Figure 3A).

Effect of integrin antagonists on cell adhesion

As previously described, consistent evidence suggests that HAC includes common focal adhesions. Actually, according with the over expression of α_5 integrin in U87MG cells, there is a good agreement between the mean number of HAC per cell revealed by vaTIRF (Figure 3D) and the mean number of focal adhesion plaques assessed by usual immunofluorescence of paxillin (Figure S1C). In addition to binding energy measurements and the high and low adhesiveness observed through HAC and LAC parameters, we further demonstrated that actin-based contractile elements preferentially take place in HAC (Figures 5B and 5E), where strong integrin-fibronectin bonds are expected. However, high adhesive contacts provided by vaTIRF display a surface somewhat higher, with a different shape, than common focal adhesion units (see Figures 1D, S5D, S5I, S1A and S1B). In fact, FA units are described as a sub-diffractive linear shape, elongated along the axis of contractile force applied by the actin cytoskeleton (2) (4). So, this suggests that FA would be incorporated in HAC. In an attempt to prove this point, the highly dynamic nature of focal adhesion plaques made experiments on fixed and transfected cells quite challenging. Membrane receptors such as integrins, actin cytoskeleton and adaptor proteins which connect actin structures to integrins within FA (such as paxillin), do not have the same spatio-temporal dynamics. This point is crucial and explains why HAC and FA colocalization is hard to establish by tagging paxillin or vinculin, as commonly proposed to observe adhesion plaques. For instance, old focal adhesion points localized with vinculin or paxillin, can subside few minutes after adhesion disassembly. In the same way, nascent vinculin or paxillin clustering can be formed shortly before the mature focal adhesion point. A recent paper clearly shows the dynamic complexity which takes place in these active zones associated to specific adhesion (7). Authors revealed a miss-match between adhesive specific contacts associated to strong pulling force and FA protein-clusters of paxillin or vinculin. Dynamic observations can be well performed with vaTIRF (38), but such kind of studies are beyond the scope of this paper. To prove that integrin-based focal adhesion is included in HAC, we decided to use soluble integrin antagonists in order to block integrin/fibronectin binding, and so FA assembly. As previously mentioned, U87MG cells exhibit on their surface $\alpha_5\beta_1$ and $\alpha_v\beta_3/\beta_5$ integrins. To inhibit integrin/fibronectin engagements (and so the related signaling pathways), two highly selective integrin antagonists were used: one specific to $\alpha_5\beta_1$ integrins, called FR, the other one specific to $\alpha_v\beta_3$ integrins, called SN (FR and SN are respectively component 1 and 3 in reference (25)). Figures S7A and S7B show the spreading of U87MG α_{5+} cells on fibronectin, treated with a mixture of FR and SN antagonists. As expected, cell/substrate contact area drastically decreases, even totally disappears. The small remaining contact area appears to be very stable over time. Thus, with antagonists, cells were unable to spread and move the same as usual when $\alpha_5\beta_1$ and $\alpha_v\beta_3$ integrins are both engaged. vaTIRF investigations on α_{5+} cells treated with these two antagonists were summarized in Figure 6. We observe that membrane height is mostly above 100 nm and the refractive index never increases, hence no HAC events were detected. Therefore, in this case, cell adhesion only arises from low adhesive contacts. This experiment clearly demonstrates that HAC appear together with integrin-based FA, thus highlighting their mutual dependency.

More interestingly, integrin antagonists offer also an excellent opportunity to identify some adhesive components involved in LAC. Indeed, fibronectin presents many binding sites, not only for integrins (RGD, PHSRN), but also for proteoglycans (typically syndecan), through its herapan sulfate (HS) binding site. Proteoglycans influence cell growth and migration, as well as actin cytoskeleton (15). They can operate as co-receptor with integrins, and they commonly associate with growth factors. For instance, syndecan-4 is well-known to promote $\alpha_5\beta_1$ integrin adhesion and stress fiber assembly in fibroblasts (52) (53). Due to the proximity of RGD and HS binding sites on fibronectin, syndecan-4 is present close to

integrin in mature FA, but not in nascent focal adhesion plaques. Like the rest of cells, U87MG human glioblastoma cells exhibit some proteoglycans that influence their adhesion and migration (54) (55). The simplest way to reveal the presence of proteoglycans in LAC, consists to observe cell spreading changes between surface coated with fibronectin and RGD (Figure S7). Since, only integrins can bind to RGD, no more adhesion is observed on RGD when cells were treated with a mix of FR and SN antagonists (Figures S7D1 and S7D2). The cell body is repelled far from the surface, and many filopodia appear, denoting the new spreading strategy adopted by the cell. Despite the fact that cell/substrate specific interactions are not possible on RGD with soluble antagonists, some cells seem to be able to spread a little bit on the surface, as shown in Figure S7D1. But time-lapse observations suggest that this dark contrast on RICM image is related to membrane undulations, probably arising from Helfrich repulsive force (56).

CONCLUSION

We propose in this paper an advanced quantification of living cells based on variable-angle TIRF nanoscopy. This technique allows us to measure the membrane height together with the refractive index of the cell cortex. We have confirmed that high and low adhesive cell/substrate contacts can be distinguished according to membrane height and the refractive index. On one hand, high adhesive contacts are related to specific adhesion engaging integrins. Specific adhesion is then characterized by a high binding energy per unit area D_S. It includes sub-diffractive focal adhesion structures and larger ones, such as those associated with actin-based platforms. These structures involve cell traction forces, as usually observed by traction force microscopy. On the other hand, low adhesive contacts are associated with a low binding energy D_S. They supposed to include several membrane components which support weak binding energy such as proteoglycans, or pure non-specific repulsive force such as glycocalyx. Compared to other techniques used to quantify cell adhesion, vaTIRF, like traction force microscopy, appears to be a non-perturbative method. For instance, techniques enabling direct force measurements related to cell adhesion strength, like AFM or flow chamber, can drastically disturb cell properties. A shear stress can induce important modification of the cell speed and contractility (47). Compared to other large field-of-view imaging techniques suited to probe cell spreading and adhesiveness, typically RICM, vaTIRFM appears to be a valuable alternative. Despite the impressive recent progress of multi-wavelength RICM (22), data processing of such interferometric technique is still complex. On the contrary vaTIRF data analysis are easy to implement. Moreover, membrane height h reconstruction with usual RICM (or multi-λ RICM), needs a perfect knowledge of the cytoplasmic refractive index. The latter is very inhomogeneous and changes drastically over time and space. Thus, h-measurement with RICM is limited to cell membrane side protrusions, such as large and flat lamellipodia (22). However, the key advantage of vaTIRFM, is that we do not need to actually know the cytoplasmic refractive index, seeing as we measure it in addition to the membrane height. On top of that, we are currently working on a new strategy based on objective back focal plane observation to improve n_{cortex} precision (57) (58) (59). Such observation can be easily implemented and provides a fine quantification of the supercritical angle which is directly given by the refractive index of the sample.

Undeniably, a large range of data is available with vaTIRF. One can determine for both strong and weak adhesion, the height of the plasma membrane, the size of the cell/substrate contact area, and the binding energy. Regarding HAC associated to strong adhesion, their individual size and their number per cell can be assessed. We also revealed how cellular contractility can influence the binding energy. As a consequence, adhesion studies conducted on U87MG cells, revealed that as expected the number of HAC per cell increases along with integrin expression level. Moreover, as expected, the higher migration speed of U87MG cells overexpressing α_5 integrins is associated with a low binding energy due to a greater contractile force. This finding was also previously observed with MDA-MB-231 cells overexpressing $\alpha_5\beta_1$ integrins (41). Moreover, our study surprisingly reveals that low adhesive contacts are also affected by integrin level and play a crucial role during adhesion. This can be explained by a crosstalk between integrins and Rho-GTPases, which controls cell's contractility through myosin motors and Arp2/3 complex (60). Actin cortex is then disturbed by integrin overexpression, as well as the plasma membrane (61).

This work opens new promising opportunities to probe integrin- or actin-mediated adhesion and migration. Further studies can be proposed when cell migration is guided along one direction according to

surface gradient of extracellular matrix proteins. This surface gradient can be obtained by electropolymerization and microfluidic (62), or by using micro-patterning. Capitalizing on all the data achievable with vaTIRF, various drugs acting on focal adhesion and actin network can be tested during migration, such as integrin antagonists or contractile forces inhibitors.

AUTHOR CONTRIBUTIONS

R.J. and D.E.A designed research; D.E.A. and R.J. performed measurements and R.J. supervised all experiments; D.E.A. and R.J. analyzed data; R.J. designed vaTIRF imaging setup; C.V. wrote data processing routines on IGOR Pro software; R.D. developed vaTIRF acquisition software; H.K. designed the integrins antagonist; D.E.A., C.V., M.L., H.K., M.D. and R.J. interpreted experiments; R.J. wrote the article.

ACKNOWLEDGMENTS

The authors thank Matthieu Piel for fruitful discussions. This work was supported by the Région Grand-Est (France), the Fonds Européen de Développement Régional (FEDER): VIVIDT, Qnanoscopy, MIRAGE projects, and the Ligue Contre le Cancer (Comité de l'Aube, France).

REFERENCES

1. Spiess, M., P. Hernandez-Varas, A. Oddone, H. Olofsson, H. Blom, D. Waithe, J. Lock , M. Lakadamyali and S. Stromblad. 2018. Active and inactive β1 integrins segregate into distinct nanoclusters in focal adhesions, J. Cell Biol. 217:1929–1940.
2. Kanchanawong, P., G. Shtengel, A. Pasapera, E. Ramko, M. Davidson, H. Hess, C. Waterman. 2010. Nanoscale architecture of integrin-based cell adhesions. Nature 468:580–584.
3. Stubb, A., C. Guzman, E. Narva, J. Aaron, T.L. Chew, M. Saari, M. Miihkinen, G. Jacquement and J. Ivaska. 2019. Superresolution architecture of cornerstone focal adhesions in human pluripotent stem cells. Nature Comm. 10:4756.
4. Hu, S., Y-H. Tee, A. Kabla, R. Zaider-Bar, A. Bershadsky and P. Hersen. 2015. Structured illumination microscopy reveals focal adhesions are composed of linear subunits. Cytoskeleton 72:235–245.
5. Rossier, O., V. Octeau, J-B. Sibarita, C. Leduc, B. Tessier, D. Nair, V. Gatterdam, O. Destaing, C. Albiges-Rizo, R. Tampe, L. Cognet, D. Choquet, B. Lounis and G. Giannone. 2012. Integrins β1 and β3 exhibit distinct dynamic nanoscale organizations inside focal adhesions. Nature cell biology 14:1057–1067.
6. Galbraith, C., M. Davidson and J. Galbraith. 2018. Coupling integrin dynamics to cellular adhesion behaviors Biology Open 7:bio036806.
7. Blakely, B.L., C.E. Dumelin, B. Trappmann, L.M. McGregor, C.K. Choi, P.C. Anthony, V.K. Duesterberg, B.M. Beker, S.M. Block, R.D. Liu and C.S. Chen. 2014. A DNA-based molecular probe for optically reporting cellular traction forces. Nature Methods 11:1229–1232.
8. Labouesse, C., J-J. Verkhovsky, A.B. Meister, C. Gabella and B. Vianay. 2015. Cell shape dynamics reveal balance of elesticity and contractility in peripheral arcs. Biophysical Journal 108:2437–2447.
9. Benard, E., J.A. Nunes, L. Limozin and K. Sengupta. 2018. T Cells on Engineered Substrates: The Impact of TCR Clustering Is Enhanced by LFA-1 Engagement. Frontiers in Immunology 9:2085.
10. Robert, P., A. Nicolas, S. Aranda-Espinoza, P. Bongrand and L. Limozin. 2011. Minimal encounter time and separation determine ligand-receptor binding in cell adhesion. Biophysical Journal 100:2642–2651.
11. Li, F., S. Redick, H. Erickson and V. Moy. 2003. Force measurements of the α5β1 integrin-fibronectin interactions. Biophysical Journal 84:1252–1262.

12. Roca-Cusachs, P., N. Gauthier, A. del Rio and M. Sheetz. 2009. Clustering of α5β1 integrins determines adhesion strength whereas αvβ3 and talin enable mechanotransduction. PNAS 106:16245–16250.
13. Liu ,Y-J., M. Le Berre, F. Lautenschaeger, P. Maiuri, A. Callan-Jones, M. Heuze, T. Takaki, R. Voituriez and M. Piel. 2015. Confinement and low adhesion induce fast amoeboid migration of slow mesenchymal cells. Cell 160:659–672.
14. Paszek, M., C. DuFort, O. Rossier, R. Bainer, J. Mouw, K. Godula, J. Hudak, J. Lakins, A.C. Wijekoon, L. Cassereau, M.G. Rubashkin, M.J. Magbanua, K. Thorn, M. Davidson, H. Rugo, J. Park, D. Hammer, G. Giannone, C. Bertozzi and V. Weaver. 2014. The cancer glycocalyx mechanically primes integrin-mediated growth and survival. Nature 511:319–325.
15. Couchman, J.R. 2010. Transmembrane signaling proteoglycans. Annu. rev. Dev. Biol. 26:89-114.
16. Evans, E., D. Berk, A. Leung and N. Mohandas. 1991. Detachment of agglutinin-bonded red blood cells. Biophysical Journal 59:849–860.
17. Albersdorfer, A., T. Feder and E. Sackmann. 1997. Adhesion-induced domain formation by interplay of long-range repulsion and short-range attraction force: a model membrane study. Biophysical Journal 73:245–257.
18. Cardoso Dos Santos, M., R. Deturche, C. Vezy and R. Jaffiol. 2016. Topography of cells revealed by variable-angle Total Internal Reflection Fluorescence microscopy. Biophysical Journal 111:1316–1327.
19. Paszek, M.J., C.C. DuFort, M.G. Rubashkin, M.W. Davidson, K.S. Thorn, J.T. Liphard and V.M. Weaver. 2012. Scanning angle interference microscopy reveals cell dynamics at the nanoscale. Nature Methods 9:825–827.
20. Bourg, N., C. Mayet, G. Dupuis, T. Barroca, P. Bon, S. Lecart, E. Fort and S. Leveque-Fort. 2015. Direct optical nanoscopy with axially localized detection. Nature Photonics 9:587–593.
21. Baronsky, T., D. Ruhlandt, B. Rouven Bruckner, J. Schafer, N. Karedla, S. Isbaner, D. Hahnel, I. Gregor, J. Enderlein, A. Janshoff and A. Chizhik. 2017. Cell-substrate dynamics of the epithelial-to-mesenchymal transition. Nano Letters 17:3320–3326.
22. Dejardin, M-J., A. Hemmerle, A. Sadoun, Y. Hamon, P-H. Puech, K. Sengupta and L. Limozin. 2018. Lamellipod reconstruction by three-dimentional reflection interference contrast nanoscopy (3D-RICN). Nano Letters 18:6544–6550.
23. Chizhik, A.M., C. Wollnik, D. Ruhlandt, N. Karedla, A.I. Chizhik, L. Hauke, D. Hähnel, I. Gregor, J. Enderlein and F. Rehfeldt. 2018. Dual-color metal-induced and Förster resonance energy transfer for cell nanoscopy. Molecular Biology of the Cell 29:846-851.
24. Janouskova, H., A. Maglott, D. Leger, C. Bossert, F. Noulet, E. Guerin, D. Guenot, S. Pinel, P. Chastagner, F. Plenat, N. Entz-Werle, J. Lehmann-Che, J. Godet, S. Martin, J. Teisinger and M. Dontenwill. 2012. Integrin α5β1 plays a critical role in resistance to temozolomide by interfering with the p53 pathway in high-grade glioma. Cancer Research 72:3463–3470.
25. Ray, A-M., F. Schaffner, H. Janouskova, F. Noulet, D. Rognan, I. Lelong-Rebel, L. Choulier, A-F. Blandin, M. Lehmann, S. Martin, T. Kapp, N. Neubauer, F. Rechenmacher, H. Kessler and M. Dontenwill. 2014. Single cell tracking assay reveals an opposite effect of selective small non-peptidic α5β1 and αv β3/β5 integrin antagonists in U87MG glioma cells. BBA General Subjects 1840:2978–2987.
26. Niederauer, C., P. Blumhardt, J. Mucksch, M. Heymann, A. Lambacher and P. Schwille. 2018. Direct characterization of the evanescent field in objective-type total internal reflection fluorescence microscopy. Optics Express 26:20492.
27. Rechenmacher, F., S. Neubauer, J. Polleux, C. Mas-Moruno, M. De Simone, E. Ada Cavalcanti-Adam, J.P. Spatz, R. Fässler and H. Kessler. 2013. Functionalizing αvβ3- or α5β1-Selective Integrin Antagonists for Surface Coating: A Method To Discriminate Integrin Subtypes In Vitro. Angew. Chem. Int. Ed. 52:1572 –1575.
28. Neubauer, S., F. Rechenmacher, R. Brimioulle, F. Saverio Di Leva, A. Bochen, T.R. Sobahi, M. Schottelius, E. Novellino, C. Mas-Moruno, L. Marinelli and H. Kessler. 2014. Pharmacophoric Modifications Lead to Superpotent αvβ3 Integrin Ligands with Suppressed α5β1 Activity. J. Med. Chem. 57:3410−3417 .
29. El Arawi, D., M. Cardoso Dos Santos, C. Vezy and R. Jaffiol. 2019. Incidence angle calibration for prismless total internal reflection fluorescence microscopy. Optics Letters 44:1710-1713.
30. Radler, J. and E. Sackmann. 1993. Imaging optical thicknesses and separation distances of phospholipid vesicles at solid surfaces. J. Phys. II 3:727–748.

31. Burmeister, J., G. Truskey and W. Reichert. 1994. Quantitative analysis of variable-angle total internal reflection fluorescence microscopy (VA-TIRFM) of cell/substrate contacts. Journal of Microscopy 173:39–51.
32. Izzard, C. and L. Lochner. 1976. Cell-to-substrate contacts in living fibroblasts: an interference reflexion study with an evaluation of the technique. J. Cell Sci. 21:129–159.
33. Izzard, C. and L. Lochner. 1980. Formation of cell-to-substrate contacts during fibroblast motility: an interference-reflexion study. J. Cell Sci. 42:81–116.
34. Bereiter-Hahn, J., C. Fox and B. Thorell. 1979. Quantitative reflection contrast microscopy of living cells. J. Cell Biology 82:767–779.
35. Andersen, M. and S. Nir. 1977. Van der Waals parameters, refractive indices and dispersion equations of spectrin, actin and other mammalian proteins. Polymer 18:867–870.
36. Jamur, M. and C. Oliver. 2010. Permeabilization of Cell Membranes. Immunocytochemical Methods and Protocols 63-66.
37. Wang, H-Y., J. Sun, L.Y. Xia, Y.H. Li, Z. Chen and F.G. Wu. 2017. Permeabilization-tolerant plasma membrane imaging reagent based on amine-rich glycol chitosan derivatives. ACS Biomater. Sci. Eng. 3:2570–2578.
38. Cardoso Dos Santos, M., C. Vezy, H. Morjani and R. Jaffiol. 2017. Single cell adhesion strength assessed with variable-angle total internal reflection fluorescence microscopy. AIMS Biophysics 4:438–450.
39. Palecek, S., J. Loftus, M. Ginsberg, D. Lauffenburger and A. Horwitz. 1997. Integrin-ligand binding properties govern cell migration speed through cell-substratum adhesiveness. Nature 385:537–540.
40. Caswell, P.T., M. Chan, A.J. Lindsay, M.W. McCaffrey, D. Boettiger and J.C. Norman. 2008. Rab-Coupling Protein Coordinates Recycling of α5β1 Integrin and EGFR1 to Promote Cell Migration in 3D Microenvironments. The Journal of Cell Biology 183:143–155.
41. Mierke, C., B. Frey, M. Fellner, M. Herrmann and B. Fabry. 2010. Integrin α5β1 facilitates cancer cell invasion through enhanced contractile forces. Journal of Cell Science 124:369–383.
42. Kuonen, F., I. Surbeck, K. Sarin, M. Dontenwill, C. Ruegg, M. Gilliet, A. Oro and O. Gaide. 2018. TGFb, Fibronectin and Integrin α5β1 Promote Invasion in Basal Cell Carcinoma. Journal of Investigative Dermatology 138:2432–2442.
43. DiMilla, P., K. Barbee and D. Lauffenburger. 1991. Mathematical model for the effects of adhesion and mechanics on cell migration speed. Biophysical Journal 60:15–37.
44. Bruinsma, Robijn. 1997. Les liaisons dangereuses: adhesion molecules do it statistically. PNAS 94:375–376.
45. Uehata, M., T. Ishizaki , H. Satoh, T. Ono, T. Kawahara, T. Morishita, H. Tamakawa, K. Yamagami, J. Inui, M. Maekawa and S. Narumiya. 1997. Calcium sensitization of smooth muscle mediated by a Rho-associated protein kinase in hypertension. Nature 389:990–994.
46. Yoshioka, K., F. Matsumura, H. Akedo and K. Itoh. 1998. Small GTP-binding protein Rho stimulates the actomyosin system, leading to invasion of tumor cells. The Journal of Biogogical Chemistry 273:5146-5154.
47. Shiu, Y.T., S. Li, W. Marganski, S. Usami, M. Schwartz, Y.L. Wang, M. Dembo and S. Chien. 2004. Rho mediates the shear-enhancement of endothelial cell migration and traction force generation. Biophysical Journal 86: 2558–2565.
48. Blanchoin, L., R. Boujemaa-Paterski, C. Sykes and J. Pastino. 2014. Actin dynamics, architectures, and mechanics in cell motility. Physiol. Rev. 94:235–263.
49. Bergert, M., S. Chandradoss, R. Desai and E. Paluch. 2012. Cell mechanics control rapid transitions between blebs and lamellipodia during migration. PNAS 109:14434–14439.
50. Cartagena-Rivera, A., J. Logue, C. Waterman and R.S. Chadwick. 2016. Actomyosin Cortical Mechanical Properties in Nonadherent Cells Determined by Atomic Force Microscopy. Biophysical Journal 110:2528–2539.
51. Chowdhury, F., I. Li, B. Leslie, S. Doganay, R. Singh, X. Wang, J. Seong, S.H. Lee, S. Park, N. Wang and T. Ha T. 2015. Single molecular force across single integrins dictates cell spreading. Integrative Biology 7:1265–1271.
52. Baciu, P.C. and P.F. Goetinck. 1995. Protein kinase C regulates the recuitment of syndecan-4 in focal contacts. Molecular Biology of the Cell 6:1503-1513.
53. Wilcox-Adelman, S.A., F. Denhez and P.F. Goetinck. 2002. Syndecan-4 modulates focal shesion kinase phosphorylation. Journal of Biological Chemistry 277:32970-32977.

54. Hu, B., L.L. Kong, R.T. Matthew and M.S. Viapiano. 2008. The proteoglycan Brevican binds to fobronectin after proteolytic cleavage and promote glioma cell motility. Journal of Biological Chemistry 283:24848-24859.
55. Frankel, P., C. Pellet-Many, P. Lehtolainen, G.M. D'Abaco, M.L. Tickner, L. Cheng and I.C. Zachary. 2008. Chondroitin sulphate-modified neuropilin 1 is expressed in human tumor cells and modulated 3D invasion in the U87MG human glioblastoma cell line through a p130Cas-mediated pathway. EMBI reports 9:983-989.
56. Marx, S., J. Schilling, E. Sackmann and R. Bruinsma. 2002. Helfrich Repulsion and Dynamical Phase Separation of Multicomponent Lipid Bilayers. Phys. Rev. Lett. 88:138102.
57. Brunstein, M., L. Roy L and M. Oheim. 2017. Near-membrane refractometry using supercritical angle fluorescence Biophysical Journal 112:1940–1948.
58. Brunstein, M., A; Salomon and M. Oheim. 2018. Decoding the information contained in fluorescence radiation patterns. ACS Nano 12:11725–11730.
59. Ferdman, B., L. Weiss, O. Alalouf, Y. Haimovich and Y. Shechtman. 2018. Ultrasensitive refractometry via supercritical angle fluorescence. ACS Nano 12:11892–11898.
60. Huveneers, S. and E. Danen. 2009. Adhesion signaling - crosstalk between integrins, Src and Rho. Journal of Cell Science 122:1059–1069.
61. Fritzsche, M., D. Li, H. Colin-York, V. Chang, E. Moeendarbary, J. Felce, E. Sezgin, G. Charras, E. Betzig and C. Eggeling. 2017. Self-organizing actin patterns shape membrane architecture but not cell mechanics. Nature Communications 8:14347.
62. Vezy, C., K. Stephan, T. Livache, A. Roget, C. Riviere, J-P. Rieu and R. Ferrigno. 2010. Coupling electropolymerization and microfluidic for the generation of surface anisotropy. Electrochemistry Communications 12:1266–1269.

Figure 1: Example of vaTIRF imaging on U87MG α_{5+} living cell in adhesion on a thin layer of fibronectin at 37°C. (A): one of the TIRF images from the stack (the plasma membrane was labeled with DiO). (B): the corresponding cell membrane topography (*h* image). (C): the refractive index n_{cortex}. (D): 2D localization of HAC (red spots on blue background), according to the dual thresholding $h \leq 70$ nm and $n_{cortex} \geq 1.365$. (E): *h*−distance histogram in grey obtained from *h* image (B) (column bin size = 5 nm). *h*−distance sub-populations corresponding to HAC and LAC, respectively in red and blue. Scale bar = 10 µm.

Figure 2: Cell/substrate distance distribution for both cell lines U87MG α_{5+} and α_{5-}. Average histograms of cell/substrate distance (black curve), obtained by summing histograms recorded on living cells in adhesion on fibronectin at 37°C, respectively for U87MG α_{5+} cells (A) and U87MG α_{5-} cells (B) (bin size 5 nm). *h*−distance distributions corresponding to HAC and LAC are respectively plotted in red (HAC) and blue (LAC). Mean heights $\langle h \rangle$ of the plasma membrane are plotted regarding the whole cell/substrate contact area (C), only for HAC (D) and for LAC (E). The color code is red for HAC and blue for LAC. 32 single cells were analyzed for each cell line. (*Wilcoxon-Mann-Whitney* test: ns not significant, error bars are ± SD).

Figure 3: HAC and LAC characteristics for single U87MG α_{5+} and α_{5-} living cells: the mean cell/substrate contact area (A), the mean HAC area (B), the mean LAC area (C), the mean HAC number per cell (D), and the scatter plot of HAC size (E) (the dashed gives us the mean value and the inset shows the corresponding box plot). Regarding HAC size, we considered only the high adhesive contacts with a size higher than the diffraction limited spot (> 0.1 μm^2). The color code is red for HAC and blue for LAC. 32 single cells were analyzed for each cell line. (*Wilcoxon-Mann-Whitney* test: $10^{-3} \lesssim$ *p $\lesssim 10^{-2}$, ***p$\lesssim 10^{-6}$, error bars are ±SD). The large error bars show the important measurement heterogeneity between each cell.

Figure 4: Potential energy *V*(*h*) and binding energy *D* of high and low adhesive contacts recorded on living cells. (A): potential energy profile, obtained according to reference (38), ▼and ▲ for respectively HAC and LAC of α_{5+} cells, ○ and □ for respectively HAC and LAC of α_{5-} cells. These data were fitted according to P. Morse function well-known in physics of diatomic molecules (red curves) (38). (B) and (C) are the binding energy D_e in k_BT unit, respectively for HAC and LAC. (D) and (E) are the binding energy given in J/m^2, denoted D_S, respectively for HAC and LAC. The color code is red for HAC and blue for LAC. 32 single cells were analyzed for each cell line. Error bars on (B) and (C) are uncertainties obtained from least-square fitting method. Error bars on (D) and (E) take into account the standard deviation of HAC and LAC area per cell.

Figure 5: (A): Effect of pulling (or traction) force F on the potential energy *V*(*h*). Black curve: the potential energy *V*(*h*) between a lipid membrane and a glass substrate, calculated by superposition of van der Waals attraction and steric repulsion due to repeller molecules (such as glycocalyx) present on the cell surface. For this calculation we considered only a lipid membrane coated with a mushroom-like polymer, in interaction with a fused silica substrate, in a saline solution, at 37°C. More details about this numerical simulation are given in Reference (38). Red curve: *V*(*h*) typical modification according to the presence of an traction force F due to actin contractile structures. The resulting potential energy must be corrected by the negative work of the pulling force ($-F \times h$). As a result, the depth of the anharmonic potential well, and so the apparent binding energy D_e measurable in vaTIRF, becomes smaller (in vaTIRF, only the beginning of the *V*(*h*)-curve is recorded). Potential energy *V*(*h*) recorded on U87MG α_{5+} living cells treated with Y27632 at 50µM (B) and LPA at 50µM (E) (● and ○ for HAC, and □ for LAC). *V*(*h*) were fitted according to P. Morse function, red curves. (C,F) and (D,G): the corresponding binding energy D_e, respectively for high adhesive contacts (in red) and low adhesive contacts (in blue). Note that the binding energies obtained for untreated cells (control) are different from those plotted in Figure 4, due to a different batch of fibronectin and small a variation of integrin expression level in the cell line. The color code is red for HAC and blue for LAC. 38 single cells were analyzed for each condition. Error bars are uncertainties obtained from least-square fitting method.

Figure 6: (A-D): typical vaTIRF investigation on U87MG α_{5+} living cell in adhesion on fibronectin at 37°C treated with a mixture of FR and SN antagonists at 20 µM each. The plasma membrane was labeled with DiO. (A): one of the TIRF images from the stack, (B): cell membrane topography, (C): n_{cortex} image, and (D): HAC/LAC image (HAC in red, LAC in blue), HAC were selected according to the dual thresholding $h \leq 70$ nm and $n_{cortex} \geq 1.36$. (E-G): HAC and LAC characteristics for single U87MG α_{5+}: the mean cell/substrate contact area (E), the mean HAC area (F) and the mean LAC area (H). FR and SN integrin antagonists were pre-diluted in DMSO, therefore data for untreated cells, control with DMSO and treated cells with 20 µM of FR and SN molecules are shown. The color code is red for HAC and blue for LAC. 30 single cells were analyzed for each condition (Wilcoxon-Mann-Whitney test: ***$p \lesssim 10^{-6}$, error bars are ± SD). Scale bar = 10µm.

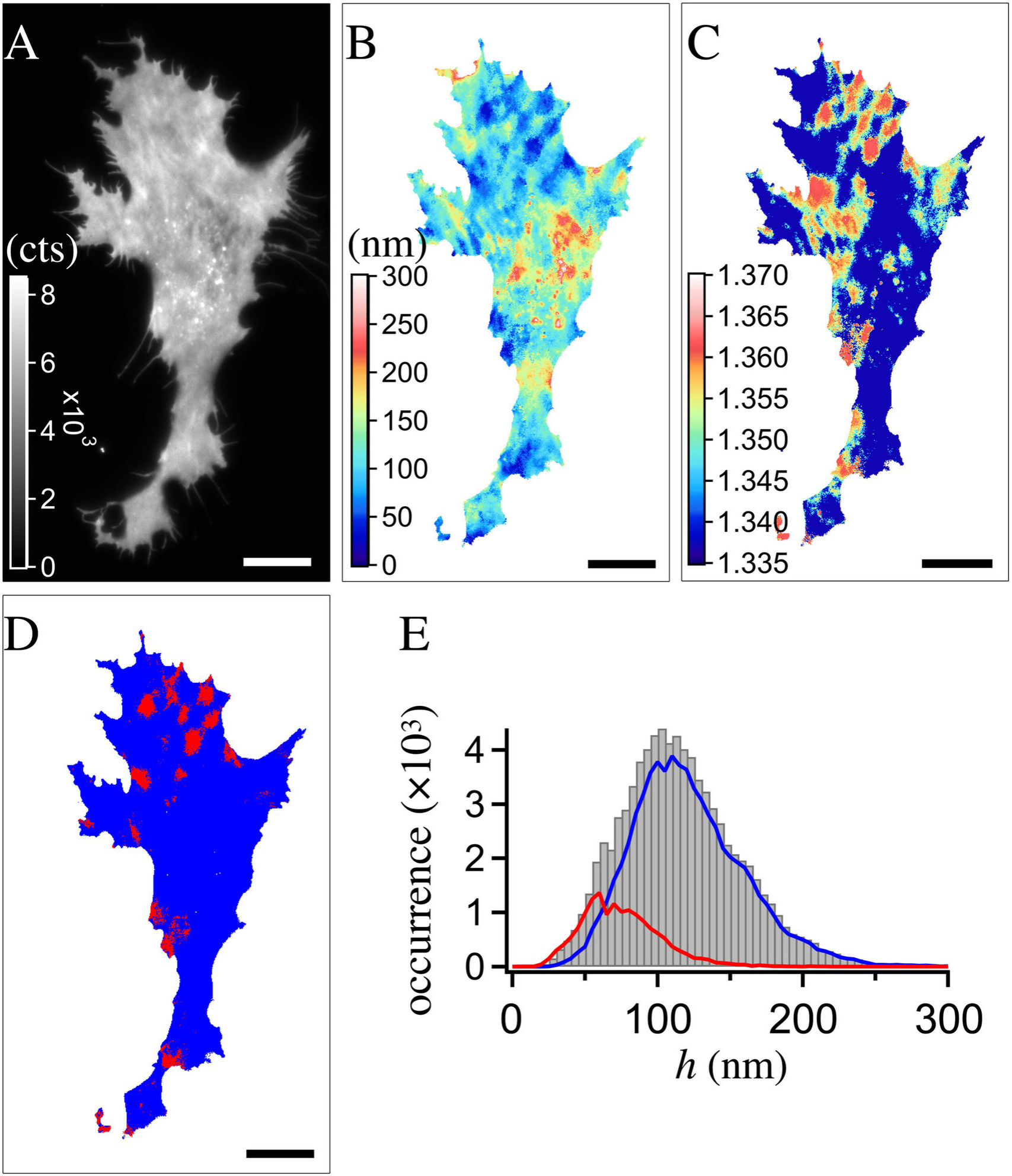
A
(cts)
8
6
4
2
0
×10³
B
(nm)
300
250
200
150
100
50
0
C
1.370
1.365
1.360
1.355
1.350
1.345
1.340
1.335
D
E
occurrence (×10³)
4
3
2
1
0
0
100
200
300
h (nm)

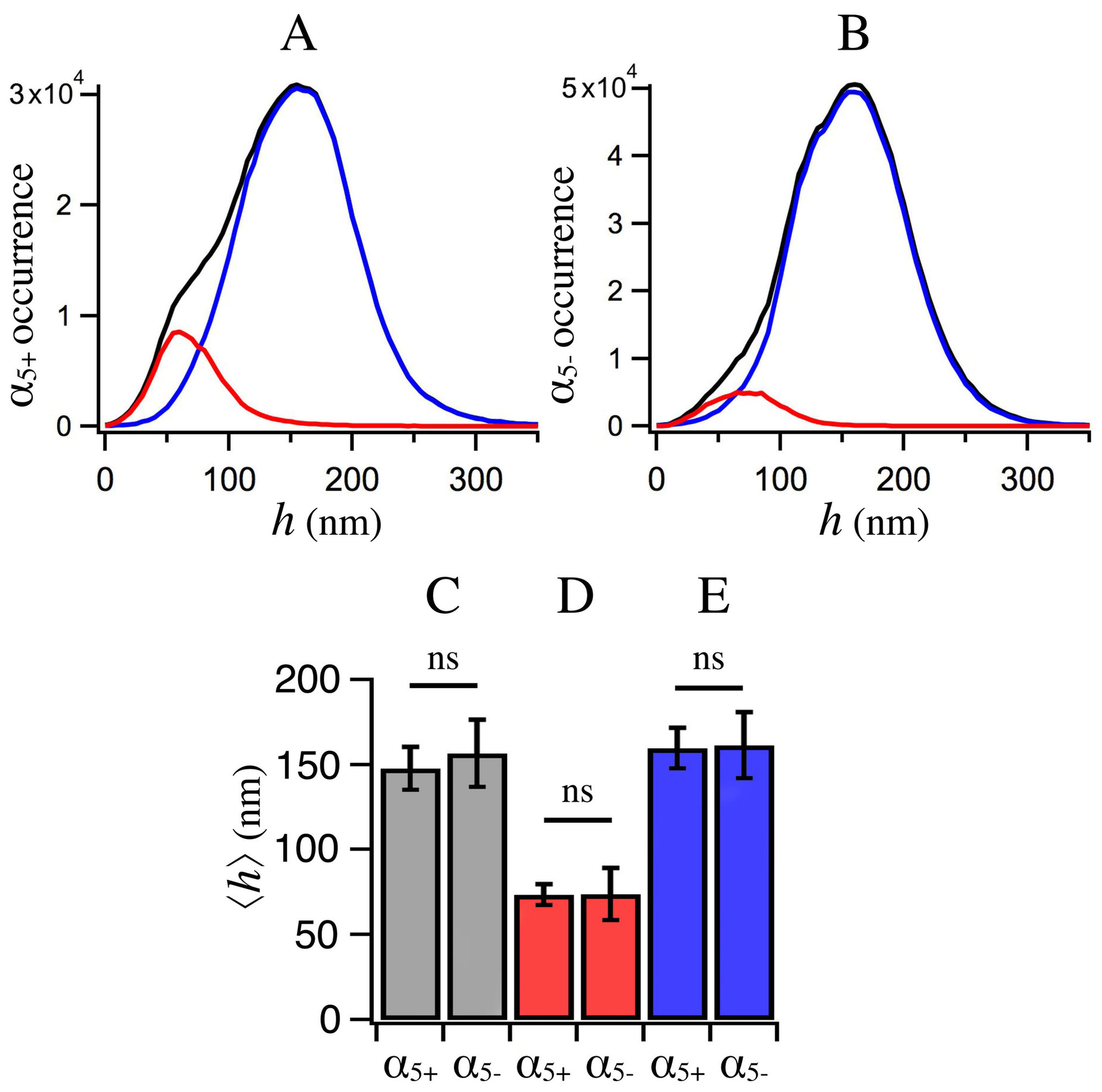
A
B
C
D
E
3x10^4
2
1
0
α5+ occurrence
5x10^4
4
3
2
1
0
α5- occurrence
0
100
200
300
h (nm)
ns
ns
ns
200
150
100
50
0
⟨h⟩ (nm)
α5+
α5-
α5+
α5-
α5+
α5-

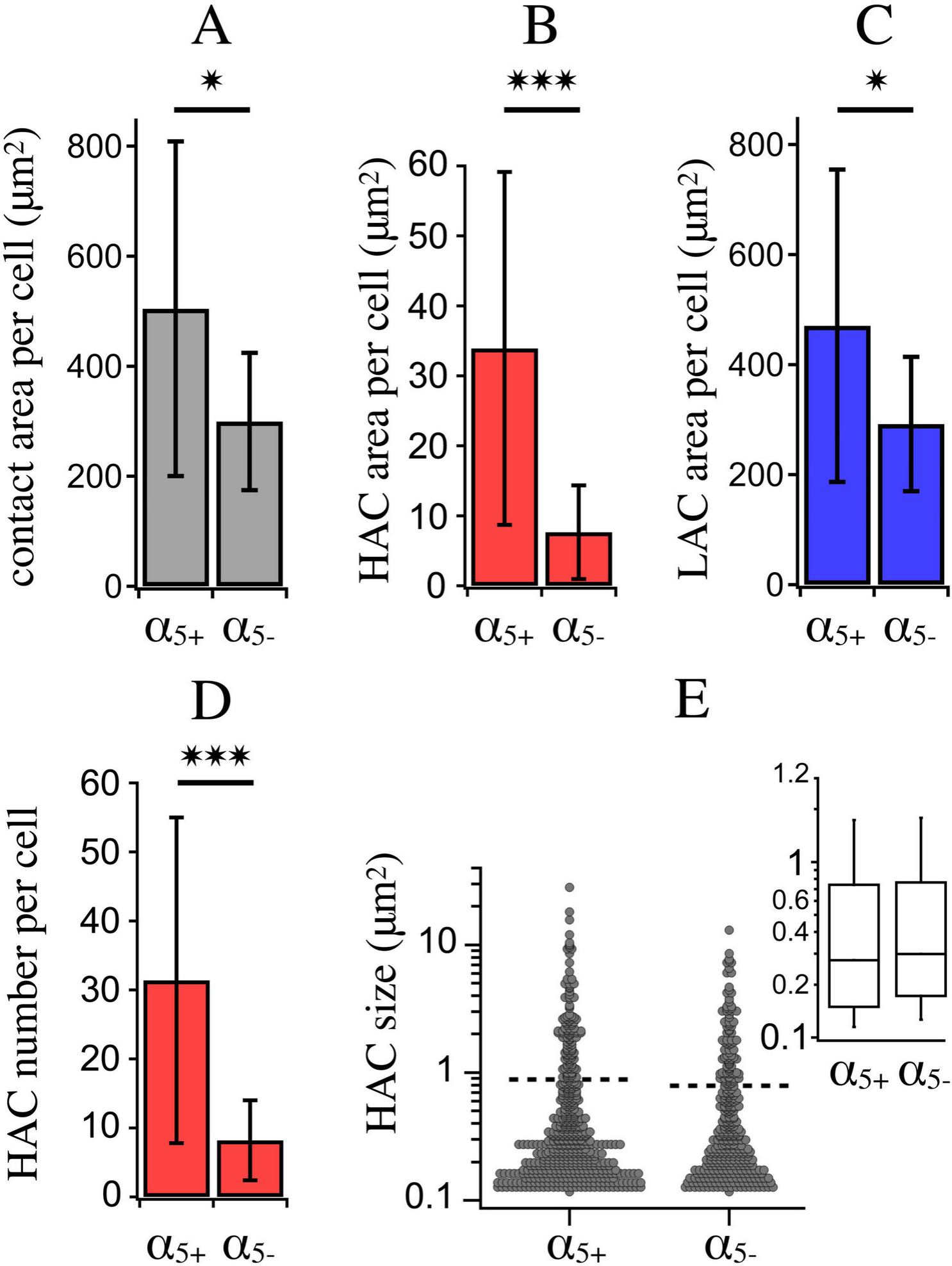
A
B
C
D
E
*
***
*
***
contact area per cell (μm²)
HAC area per cell (μm²)
LAC area per cell (μm²)
HAC number per cell
HAC size (μm²)
0
200
400
600
800
10
20
30
40
50
60
0.1
1
10
0.2
0.4
0.6
1.2
α5+
α5-

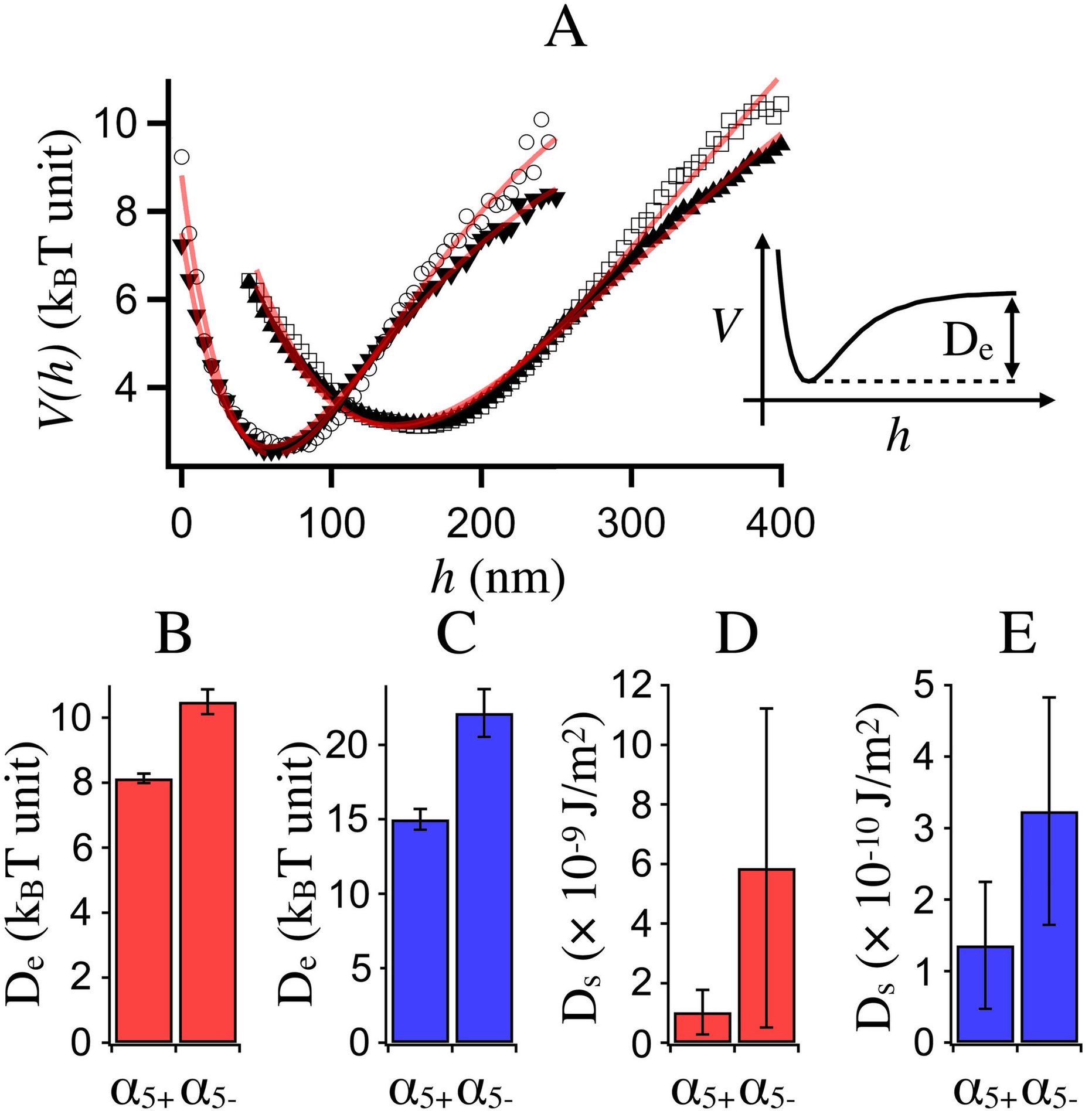
A
V(h) (kBT unit)
h (nm)
V
De
h
B
C
D
E
De (kBT unit)
Ds (× 10-9 J/m2)
Ds (× 10-10 J/m2)
α5+ α5-

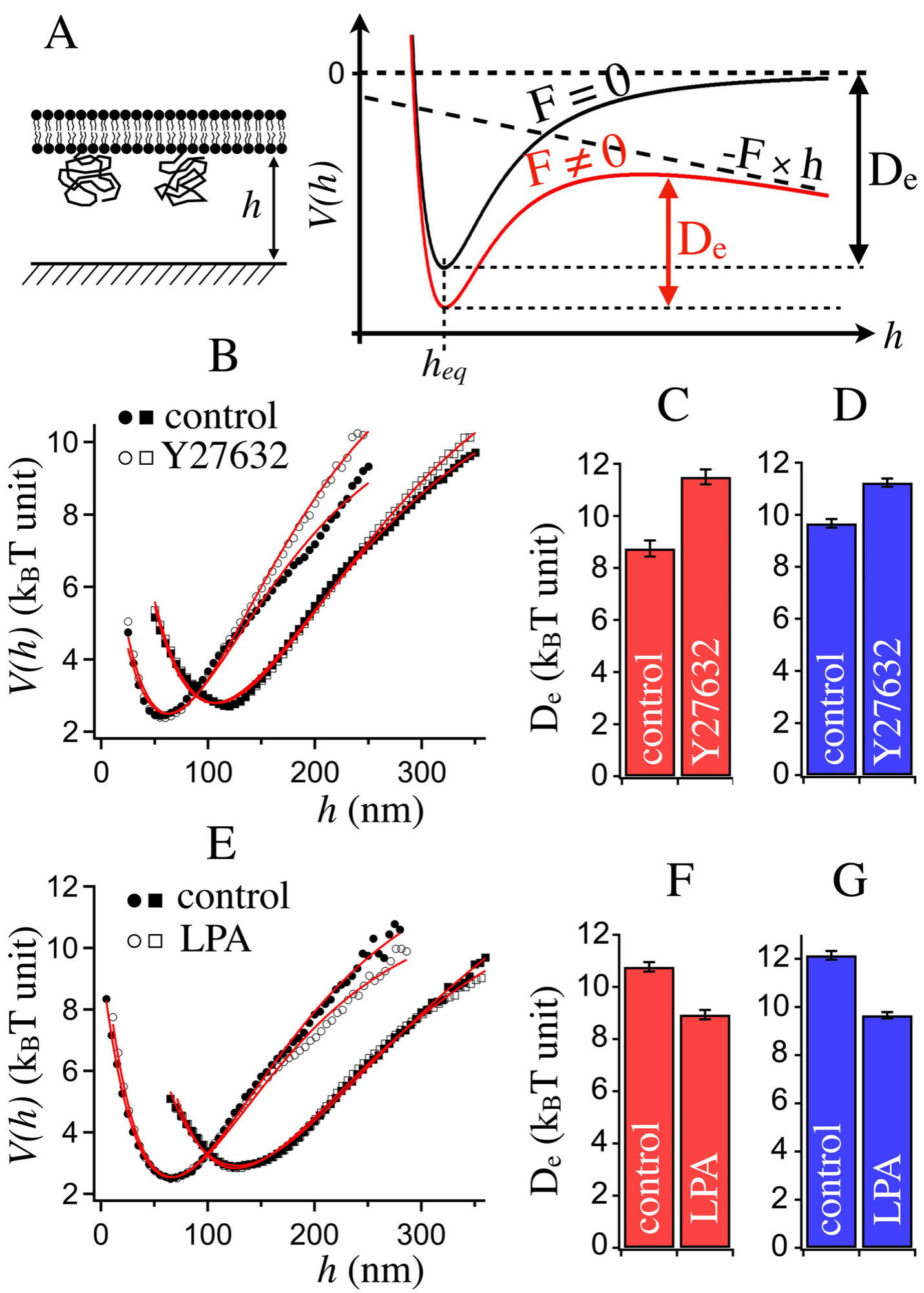
A
h
0
F ≡ 0
F ≠ 0
-F × h
V(h)
De
De
h
heq
B
control
Y27632
V(h) (kBT unit)
h (nm)
C
D
De (kBT unit)
control
Y27632
control
Y27632
E
control
LPA
V(h) (kBT unit)
h (nm)
F
G
De (kBT unit)
control
LPA
control
LPA

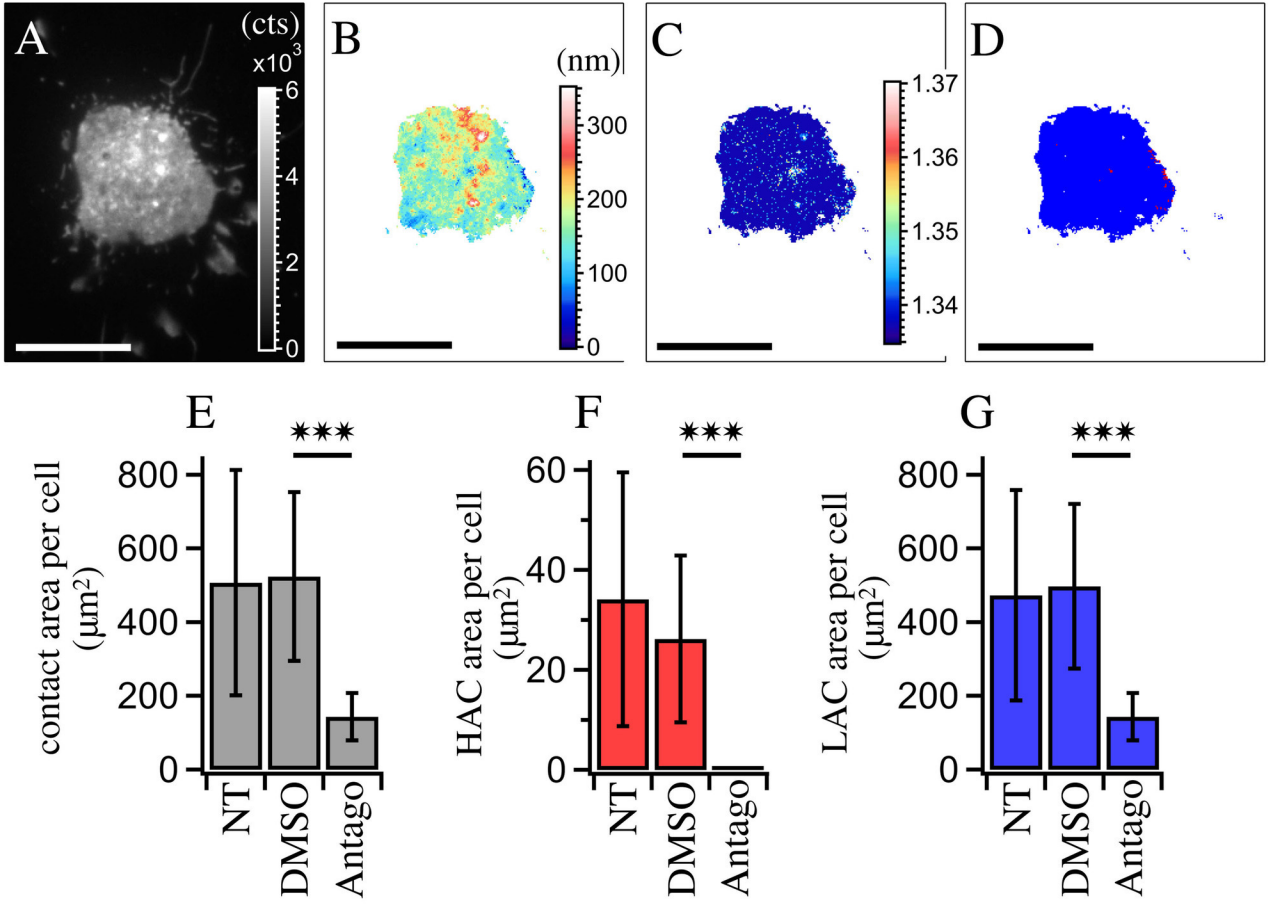
A
(cts)
x10^3
6
4
2
0
B
(nm)
300
200
100
0
C
1.37
1.36
1.35
1.34
D
E
***
contact area per cell (μm²)
800
600
400
200
0
NT
DMSO
Antago
F
***
HAC area per cell (μm²)
60
40
20
0
NT
DMSO
Antago
G
***
LAC area per cell (μm²)
800
600
400
200
0
NT
DMSO
Antago